Magnetic-field-tunable anisotropic blackbody radiation and condensation of slow thermal light in dynamical axion insulators

E. Kochems,[1] G. Quintero Angulo,[1,2] R. Egger,[1] C. Müller,[1] and S. Villalba-Chávez[1,*]
[1]Institut für Theoretische Physik, Heinrich-Heine-Universität Düsseldorf, Universitätsstraße 1, 40225 Düsseldorf, Germany
[2]Departamento de Física Teórica, Facultad de Física, Universidad de la Habana, San Lázaro y L, Vedado, La Habana 10400, Cuba

(Received 18 July 2024; revised 20 May 2025; accepted 21 July 2025; published 29 September 2025)

Thermal radiation features of dynamical axion insulators, which are characterized by an antiferromagnetic order with simultaneously broken time-reversal and space-inversion symmetries, are investigated. Planck's radiation law is shown to exhibit remarkable anisotropic behavior as a result of the strong dispersion caused by the light-matter interaction. A crossover scenario at low temperature is identified and an associated phase highly populated by slow thermal photons is revealed. We show that the asymmetry degree of the heat radiation and its angular distribution can be controlled via a magnetic field, paving the way toward a directional-tunable mechanism for thermal quantum manipulation and storage. Analogies are drawn with the expected behavior of blackbody radiation in the core of neutron stars.

DOI: 10.1103/sh8w-rk4b

I. INTRODUCTION

Solving the strong CP problem through the Peccei-Quinn mechanism led to the emergence of the QCD axion [1–3] and has since been a paradigm for the broader class of axions occurring in various standard model extensions [4–12], some of which put them forward as viable candidates for nonbaryonic dark matter [13–17]. While the original QCD axion was ruled out shortly after its prediction [18,19], experimental endeavors toward the detection of axionlike particles are nowadays being carried out worldwide [20,21], based predominantly on the axion-diphoton coupling that characterizes the theoretical framework of axion electrodynamics (AED) [22]. Despite compelling theoretical arguments supporting their existence, no axion has been detected to date, thus suggesting a feeble interplay between these elusive particles and the well-established standard model constituents.

With the plausible realization of dynamical axionlike fields in topological insulators with broken space-inversion and time-reversal symmetries, an enticing landscape to study axion physics has been opened [23]. Indeed, dynamical axion insulators (DAIs), such as the already synthesized $MnBi_2Te_4$ flakes [24–28], constitute suitable platforms for proof-of-principle tests of various phenomena on which axion searches rely. Moreover, the intrinsic characteristics of the medium, such as stiffness and topology, along with the knowledge of the associated axion quasiparticle mass, make DAIs ideal for investigating phenomena beyond the perturbative regime that the counterpart of particle physics justifiably utilizes. Theoretical studies in this direction have revealed a few emerging phenomena closely linked to the hallmark medium's magnetoelectric response [29–33] and in line DAI-based methods to detect dark-matter axions have been proposed [28,34,35].

The thermal radiation properties of DAIs are of particular interest to nuclear astrophysics. This is due to their potential to offer significant insights into blackbody radiation within the magnetic dual chiral density wave (MDCDW) phase of dense quark matter [36–40], which is presently regarded as a plausible model for characterizing the cores of neutron stars and magnetars [41–43]. Axion electrodynamics rules light-matter interaction in the MDCDW phase, just as it does in DAIs. As a result, the propagation of electromagnetic waves in both scenarios is significantly influenced by axion-polariton states [44,45]. While some astrophysical consequences of these hybridized states have been discussed, their significance for the stellar thermal properties remains uncertain. However, the existing analogy between the MDCDW phase and DAIs renders the latter an ideal playground for emulating hitherto unobserved phenomena of heat radiation under extreme conditions.

Moreover, the realization of cavity-based axion polaritons [46] could benefit the quantum control of light-matter interaction over other widely studied systems, like qubits in superconducting circuits and cavity optomechanical oscillators [47,48]. The primary reasons for these prospects stem from DAI's seemingly favorable cooling feature and the opportunity to magnetically control the interaction strength [49]. However, high field strengths could induce noticeable changes in the axion quasiparticle mass and thus modify the critical temperature for condensation of the massive branch of the axion-polariton ensemble, making it difficult to cool to the ground state even if it is characterized by a low population. The question raised is whether further repercussions linked

*Contact author: villalba@uni-duesseldorf.de

with the breakdown of spatial isotropy may have nontrivial effects on the system's thermodynamic control.

In this paper we show that, near the critical boundary between the antiferromagnetic and paramagnetic phases, the axion-polariton state renders Planck's radiation law exhibiting a field-tunable anisotropy. This remarkable feature enables the control of direction-dependent macroscopic properties of thermal radiation under equilibrium conditions. Our research uncovers qualitatively novel characteristics of DAIs, including a many-body condensate of slowly moving photons distinguished by low-dimensional transport of energy. Likewise, it is indicated, based on the aforementioned analogy, which of these characteristics prevail in the blackbody radiation of the MDCDW phase of dense quark matter.

The paper is structured in the following form. In Sec. II, thermal field theory methods are employed to derive the partition function and Helmholtz free energy of the axion-photon ensemble interacting with a constant external magnetic field. The resulting formulas are subsequently utilized in Sec. III to obtain the modified Planck law, from which the nature of blackbody radiation in DAIs is elucidated. Our conclusions are given in Sec. IV. Details of the calculations and further information on the optical features of thermal radiation are provided in the Appendix.

II. THERMAL-FIELD-THEORY APPROACH

Let us consider a DAI sample characterized by a volume $V = L_x L_y L_z$. We describe the equilibrium blackbody radiation inside the insulator using AED. By adopting rationalized Gaussian units with $c = \hbar = k_B = \epsilon_0 = 1$, this theoretical framework is characterized by the action [23]

$$\Gamma = \int d^4x\bigg(4\pi J g^2[(\partial_t\delta\theta)^2 - (v_i\partial_i\delta\theta)^2 - m^2\delta\theta^2] + \frac{1}{2}(\boldsymbol{D}\cdot\boldsymbol{E} - \boldsymbol{H}\cdot\boldsymbol{B}) + \frac{\alpha}{\pi}(\bar{\theta} + \delta\theta)\boldsymbol{E}\cdot\boldsymbol{B}\bigg). \tag{1}$$

Here $\boldsymbol{D} = \epsilon\boldsymbol{E}$ and $\boldsymbol{H} = \mu^{-1}\boldsymbol{B}$ are the electric and magnetic displacement vectors, with ϵ and μ denoting the respective dielectric constant and magnetic permeability, with material stiffness J, constant g, and $\alpha = e^2/4\pi$ referring to the fine-structure constant. We note that the static axion field $\bar{\theta}$ takes $\bar{\theta} = \pi$ in time-reversal invariant topological insulators, whereas $\bar{\theta} = 0$ in topologically trivial insulators [33]. In Eq. (1), $v_{i=x,y,z}$ stands for the group velocity components of the free low-energy spin wave $\delta\theta$ with $|\delta\theta| < \bar{\theta}$, whereas m refers to its mass. This dynamical field is the projection of the fluctuation of the spontaneous antiferromagnetic order parameter, i.e., Néel's field, onto the crystallographic anisotropy axis of the magnetic topological insulator [35]. In the following, we employ a rescaled version of $\delta\theta$, $\sqrt{8\pi J g^2}\delta\theta \to \phi$, which results in a multiplicative renormalization of the gauge coupling $\alpha \to \alpha/\sqrt{8\pi J g^2}$. We remark that Eq. (1) provides a reliable physical description when the energy and momentum of low-energy excitations are significantly below the material's bulk gap $\Delta \sim O(0.1)$ eV and the upper momentum limit $\Lambda_i \sim \Delta/v_i$, respectively.

Heat radiation will be identified with small-amplitude electromagnetic waves $a_\mu(t,\boldsymbol{x})$ describing the linear response of the system to the presence of a constant magnetic background $\boldsymbol{B} = (0, 0, B)$. As a consequence, we will focus on the action that results from Eq. (1) when the electromagnetic fields $\boldsymbol{E}$ and $\boldsymbol{B}$ are replaced by $\boldsymbol{e} = -\nabla a_0 - \partial\boldsymbol{a}/\partial t$ and $\boldsymbol{B} + \boldsymbol{b}$ with $\boldsymbol{b} = \nabla\times\boldsymbol{a}$, respectively, and only nontrivial bilinear combinations in $a_\mu(t,\boldsymbol{x})$ are retained,

$$S = \int d^4x\bigg(-\frac{\boldsymbol{B}^2}{2\mu} + \frac{1}{2}[\boldsymbol{e}^2 - c'^2\boldsymbol{b}^2] + \kappa\phi\boldsymbol{e}\cdot\boldsymbol{B} + \frac{1}{2}[(\partial_t\phi)^2 - (v_i\partial_i\phi)^2 - m^2\phi^2] + \frac{\alpha\bar{\theta}(z)}{\pi\sqrt{\epsilon}}\boldsymbol{e}\cdot\boldsymbol{B}\bigg), \tag{2}$$

where the rescaling $a_\mu(t,\boldsymbol{x}) \to a_\mu(t,\boldsymbol{x})/\sqrt{\epsilon}$ has been carried out, $c' = 1/\sqrt{\epsilon\mu}$ denotes the speed of light in the medium, and $\kappa = \alpha/\sqrt{(2\pi)^3 J g^2\epsilon}$ is the coupling strength between $\phi(t,\boldsymbol{x})$ and $a_\mu(t,\boldsymbol{x})$ mediated by $\boldsymbol{B}$. Observe that, to account for the topological charges on the surfaces perpendicular to $\boldsymbol{B}$, the static axion field $\bar{\theta}$ has been promoted to a z-dependent function, i.e., $\bar{\theta} \to \bar{\theta}(z) = \bar{\theta}\,\Theta(L_z/2 + z)\Theta(L_z/2 - z)$, with $\Theta(x)$ denoting the unit-step function [$\Theta(x) = 1$ if $x \geqslant 0$ and $\Theta(x) = 0$ otherwise].

Establishing the corresponding Helmholtz free energy $\mathscr{F} = -\beta^{-1}\ln\mathcal{Z}$ requires adopting the imaginary-time formalism $t \to -i\tau$ with $0 \leqslant \tau \leqslant \beta$ and $\beta = T^{-1}$ denoting the inverse temperature. In this context, the boson fields $\phi(x)$ and $a_\mu(x)$ with $x_\mu = (\boldsymbol{x}, \tau)$ and $\mu = 1, 2, 3, 4$ are promoted to periodic functions in the variable τ. The calculation of the required partition function can be carried out by extending the covariant Faddeev-Popov ansatz [50,51] to the case under consideration:

$$\int \mathcal{D}\chi\, \delta(\mathscr{G}[{}^\chi a_\mu])\det(\delta\mathscr{G}[{}^\chi a_\mu]/\delta\chi)_{\chi=0} = 1.$$

Here the gauge-transformed field is ${}^\chi a_\mu = a_\mu + \partial_\mu\chi$ and the gauge-fixing function $\mathscr{G}[a_\mu] = -c'^2\nabla\cdot\boldsymbol{a} - \partial_\tau a_4 + s$, with $s(x)$ denoting an arbitrary space-time depending scalar. Moreover, $\det(\delta\mathscr{G}[{}^\chi a_\mu]/\delta\chi)_{\chi=0} = \det(-\Box_{x,\tilde{x}})$ is the Faddeev-Popov determinant with $\Box_{x,\tilde{x}} \equiv \partial_x^2\delta^4(x - \tilde{x})$ and $\partial^2 = c'^2\nabla^2 + \partial_\tau^2$. As such, the partition function is independent of $s(x)$. Upon weighting it with the Gaussian factor $\exp(-\frac{1}{2\zeta c'^2}\int_X d^4x\, s^2)$, with $\int_X d^4x \equiv \int_0^\beta d\tau\int_V d^3x$ and a gauge-fixing parameter ζ, and integrating functionally over $s(x)$, the gauge-fixing term rises to the exponent and

$$\mathcal{Z} = \exp\left(-\frac{\beta V}{2\mu}B^2\right)\mathcal{Z}_{\rm AED}, \qquad \mathcal{Z}_{\rm AED} = \det(-\Box_{x,\tilde{x}})\int_{\rm periodic}\mathcal{D}a\,\mathcal{D}\phi\, e^{-S_{\rm E}}. \tag{3}$$

Here $S_{\rm E}$ is the Euclidean action resulting from Eq. (1) combined with the gauge-fixing term.

The functional integrations in Eq. (3) can be straightforwardly calculated owing to the integrand's Gaussian nature. This feature guarantees indeed that the contribution of small amplitude waves dominates over the remaining ones. Upon carrying out the one over $\phi(x)$ and adopting the Feynman gauge $\zeta = 1$, we find

$$\mathcal{Z}_{\rm AED} \propto \det(-\Box_{x,\tilde{x}})\left[\det\left(-\Box^{v}_{x,\tilde{x}} + m^2_{x,\tilde{x}}\right)\right]^{-1/2} \int \mathcal{D}a \exp\left[-\int_X d^4x\left(\int_X d^4\tilde{x}\frac{1}{2}a_\alpha(x)D^{-1}_{\alpha\beta}(x,\tilde{x})a_\beta(\tilde{x}) + \varrho(z)a_4(x)\right)\right]. \quad (4)$$

Here $\varrho(z) = \frac{\alpha B}{\sqrt{\epsilon}}[\delta(z + L_z/2) - \delta(z - L_z/2)]$ is the topological charge density, whereas $D^{-1}_{\alpha\beta}(x,\tilde{x}) = -\Box_{x,\tilde{x}}\,\tilde{\delta}_{\alpha\beta} + \Pi_{\alpha\beta}(x,\tilde{x})$ denotes the inverse photon propagator with $\tilde{\delta}_{\alpha,\beta} = \mathrm{diag}(1, 1, 1, 1/c'^2)$ and

$$\Pi_{\alpha\beta}(x,\tilde{x}) = -\kappa^2\tilde{F}_{\alpha\sigma}\left[\partial^x_\sigma\partial^{\tilde{x}}_\mu\Delta_{\rm E}(x,\tilde{x})\right]\tilde{F}_{\mu\beta}$$

the polarization tensor [see Fig. 1(a)] mediated by the Euclidean axion propagator $\Delta_{\rm E}(x,\tilde{x})$ [52,53]. Here $\tilde{F}_{\alpha\beta} = \frac{1}{2}\varepsilon_{\alpha\beta\mu\nu}F_{\mu\nu}$, with $\varepsilon_{1234} = 1$. The components of the external electromagnetic tensor $F_{\alpha\beta}$ are $F_{j4} = 0$ and $F_{j\ell} = -\epsilon_{j\ell k}B_k$. In Eq. (4) we have used the shorthand notation $\Box^v_{x,\tilde{x}} \equiv [\partial^2_\tau + (v_i\partial_i)^2]\delta^4(x - \tilde{x})$ and $m^2_{x,\tilde{x}} \equiv m^2\delta^4(x - \tilde{x})$. Next we express $a_\alpha(x)$ as a Fourier series $a_\alpha(x) = \sqrt{\beta/V}\sum_{n,\boldsymbol{q}} a_\alpha(n,\boldsymbol{q})\exp[i(\omega_n\tau + \boldsymbol{q}\cdot\boldsymbol{x})]$, where $\omega_n = 2n\pi/\beta$ are the bosonic Matsubara's frequencies, and carry out the integration. As a consequence,

$$\mathcal{Z}_{\rm AED} = \exp\left(-\varsigma\frac{\alpha^2}{\pi^3\epsilon}\bar{\theta}^2\beta VB^2\right)\prod_{n,\boldsymbol{q}}\left[\beta^2\left(\omega_n^2 + \omega_o^2\right)\right]\left[\beta^2\left(\omega_n^2 + v_i^2q_i^2 + m^2\right)\right]^{-1/2}\left\{\beta^8\det\left[\tilde{\delta}_{\alpha\beta}\left(\omega_n^2 + \omega_o^2\right) + \Pi_{\alpha\beta}(-q)\right]\right\}^{-1/2}, \quad (5)$$

where $\varsigma = 1 - \mathrm{Si}(1) + \pi/2 - \cos(1) \approx 1.084\,410\,951$, with $\mathrm{Si}(x)$ referring to the sine integral function. Here $\omega_o = c'|\boldsymbol{q}|$ is the ordinary photon dispersion law in the medium. In Eq. (5) an unessential proportionality factor has been ignored and the Fourier transform of the polarization tensor reads $\Pi_{\alpha\beta}(\tilde{q}, q) = \delta_{\tilde{q},-q}\mathcal{P}_{\alpha\beta}(q)$, where $\Pi_{\alpha\beta}(q) = \kappa^2\Delta_{\rm E}(q)\tilde{F}_{\alpha\lambda}q_\lambda\tilde{F}_{\beta\sigma}q_\sigma$, with $\Delta_{\rm E}(q) = (\omega_n^2 + v_i^2q_i^2 + m^2)^{-1}$ and $q_\mu = (\boldsymbol{q}, \omega_n)$.

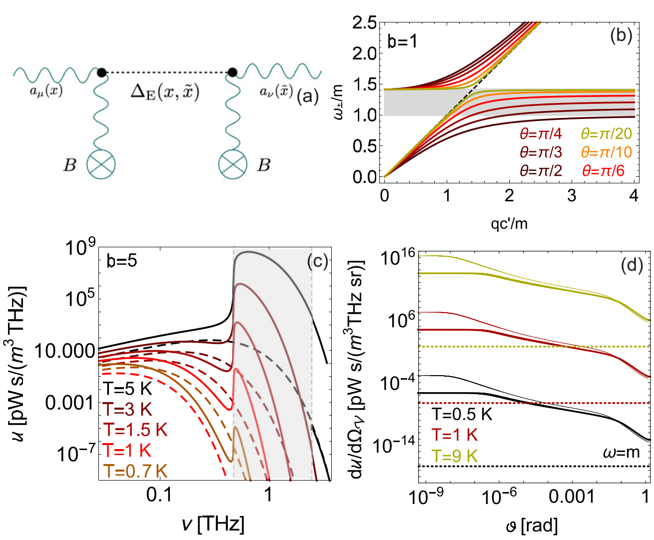

FIG. 1. (a) Polarization tensor in AED. (b) Dispersion relations. The dashed line is linked to the ordinary photon ω_o, whereas the gray band shows the maximum gap. While the lower (massless) branch is associated with extraordinary photons ω_-, the upper (massive) one is linked to axions ω_+. (c) Blackbody spectrum. The gray band shows the maximum gap at $\mathfrak{b} = 5$. The dashed (solid) curves display the ordinary (extraordinary) photon spectrum. The black solid curve in the lower right corner depicts the axionlike spectrum at $T = 5$ K. (d) Angular distribution of the internal energy density linked to extraordinary photons at $\omega = m$ $[d\Omega_v \equiv d\varphi d\cos(\vartheta)]$. Curves sharing a color are linked to a common temperature at $\mathfrak{b} = 1$ (thick) and $\mathfrak{b} = 5$ (thin). The dotted lines show the contributions of the ordinary mode.

Next we substitute Eq. (5) into Eq. (3) and obtain, from the resulting expression for $\mathcal{Z}$, the Helmholtz free energy. After carrying out the sum over the Matsubara frequencies we find

$$\mathscr{F} = \frac{V}{2\mu}B^2\left(1 + 2\varsigma\frac{\alpha^2}{\pi^3}\frac{\mu}{\epsilon}\bar{\theta}^2\right) + \mathscr{F}_{\rm vac} + \mathscr{F}_{\rm st}, \quad (6)$$

with $\mathscr{F}_{\rm vac} = \frac{1}{2}V\sum_i\int_\Lambda\frac{d^3q}{(2\pi)^3}\omega_i$ the vacuum contribution and $\mathscr{F}_{\rm st} = \frac{V}{\beta}\sum_i\int_\Lambda\frac{d^3q}{(2\pi)^3}\ln(1 - e^{-\beta\omega_i})$ the statistical one. Here we take the continuum limit $V \to \infty$, bounding the integration domain to a region $\boldsymbol{\Lambda} = (\Delta/v_x, \Delta/v_y, \Delta/v_z)$, where the low-energy description (1) applies. In $\mathscr{F}_{\rm vac}$ and $\mathscr{F}_{\rm st}$, the latin index i runs over $i = $ o, $\pm$, covering the massless (photonlike excitations) and massive branches of the polariton state, which are linked with the extraordinary (ω_-) and axionlike (ω_+) dispersion relations

$$\omega^2_\mp = \tfrac{1}{2}(\omega_o^2 + w_*^2) \mp \tfrac{1}{2}\sqrt{\left(\omega_o^2 - w_*^2\right)^2 + 4m^2\mathfrak{b}^2c'^2q_\perp^2}, \quad (7)$$

respectively. Here $q_\perp$ is the momentum perpendicular to $\boldsymbol{B}$ and $w_* = (v_i^2q_i^2 + m_*^2)^{1/2}$, with $m_* = m(1 + \mathfrak{b}^2)^{1/2}$ the dressed axion mass, $\mathfrak{b} = B/B_0$, and $B_0 = m/\kappa$ denoting the characteristic magnetic-field scale of AED.

III. RESULTS AND DISCUSSION

Our numerical evaluation relies on the benchmark parameters estimated for the antiferromagnetic phase of $(Bi_{1-x}Fe_x)_2Se_3$ with a nominal doping concentration approximately equal to 3.5% [23,54]. In this case, the factor $Jg^2 \approx 450$ eV^2 and the dynamical axion mass can reach values as small as $m \approx 2$ meV near the critical boundary between the antiferromagnetic and paramagnetic phases. The values of these parameters are generally T dependent [55,56], lifting the typical mass of the axionlike quasiparticle to $m \sim O(1)$ eV far from the phase boundary [56,57]. Conversely, in the vicinity of the critical limit, the mass changes with the doping concentration but varies very slowly with temperature, enabling us to treat the benchmark mass as a constant [55]. Moreover, the estimated dielectric constants in this material are $\epsilon \approx 25$ and $\mu \sim 1$, leading to a speed of light $c' \approx 0.2$

and a characteristic magnetic-field scale $B_0 \approx 2.35$ T that can easily be surpassed. Hereafter, we will consider the velocity components of a free axion to be equal and of the order of the spin wave speed, which we take as $v_{x,y,z} = v_s = 10^{-4}$ [35,58,59]. Figure 1(b) shows the mutual repelling behavior of the resulting dispersion relations [see Eq. (7)] that characterize the axion-polariton state. Here $\theta \in [0, \pi]$ is the angle between the wave vector $\boldsymbol{q}$ and $\boldsymbol{B}$.

At this point, we find it convenient to determine the inverse relations $|\boldsymbol{q}|_\pm = n_\pm \omega$ with $n_\pm$ referring to the refraction indices, explicitly,

$$n_\pm^2(\omega,\theta) = \frac{1}{2v_s^2}\left(1 + \frac{v_s^2}{c'^2} - \frac{m_*^2(\theta)}{\omega^2}\right) \mp \frac{1}{2v_s^2}\sqrt{\left(1+\frac{v_s^2}{c'^2} - \frac{m_*^2(\theta)}{\omega^2}\right)^2 - 4\frac{v_s^2}{c'^2}\left(1-\frac{m_*^2}{\omega^2}\right)}, \tag{8}$$

where $m_*^2(\theta) \equiv m^2[1 + \mathfrak{b}^2\cos^2(\theta)]$ and as before the negative (positive) subindex is linked to the massless (massive) branch because $\lim_{\omega\to 0} |\boldsymbol{q}|_- = 0$, whereas $\lim_{\omega\to m_*} |\boldsymbol{q}|_+ = 0$. The expressions for $|\boldsymbol{q}|_\pm$ as well as $\omega_\pm$ in Eq. (7) are solutions of the dispersion equation

$$\omega^4 - \omega^2(\omega_o^2 + w_*^2) + \omega_o^2 w_*^2 - m^2\mathfrak{b}^2 c'^2 |\boldsymbol{q}|^2 \sin^2(\theta) = 0, \tag{9}$$

from which the relevant group-velocity components are obtained. The ones perpendicular and parallel to $\boldsymbol{B}$ read

$$\begin{aligned} v_{\perp,i}(\omega,\theta) &= \left|\frac{\partial \omega_i}{\partial q_\perp}\right|_{|\boldsymbol{q}|\to n_i\omega} \\ &= c'^2 n_i \sin(\theta)\frac{\omega^2\left(1 + \frac{v_s^2}{c'^2} - 2v_s^2 n_i^2\right) - m^2}{2\omega^2\left[1 - \frac{1}{2}\left(1 + \frac{v_s^2}{c'^2}\right)\frac{n_i^2}{n_o^2}\right] - m_*^2}, \\ v_{\parallel,i}(\omega,\theta) &= \left.\frac{\partial \omega_i}{\partial q_\parallel}\right|_{|\boldsymbol{q}|\to n_i\omega} \\ &= c'^2 n_i \cos(\theta)\frac{\omega^2\left(1 + \frac{v_s^2}{c'^2} - 2v_s^2 n_i^2\right) - m_*^2}{2\omega^2\left[1 - \frac{1}{2}\left(1 + \frac{v_s^2}{c'^2}\right)\frac{n_i^2}{n_o^2}\right] - m_*^2}, \end{aligned} \tag{10}$$

where the replacement $|\boldsymbol{q}| \to n_i\omega$ must be carried out only after the differentiation and $i = \pm$. The derivatives in Eq. (10) can easily be established by implicitly differentiating Eq. (9) with respect to the variables $q_{\perp,\parallel}$.

A. Anisotropic blackbody spectra

In order to assess how the field-dependent dispersion phenomenon affects the medium's thermal properties, we first focus on the blackbody spectra. To this end, we primarily investigate the internal energy density

$$\begin{aligned} \mathcal{U} &= \frac{1}{V}\frac{\partial(\beta\mathscr{F})}{\partial\beta} = \frac{B^2}{2\mu}\left(1 + 2\varsigma\frac{\alpha^2}{\pi^3}\frac{\mu}{\epsilon}\bar{\theta}^2\right) + \sum_i \mathcal{U}_i, \\ \mathcal{U}_i &= \int_\Lambda \frac{d^3q}{(2\pi)^3}\frac{\omega_i}{\exp(\beta\omega_i) - 1} + \frac{1}{2}\int_\Lambda \frac{d^3q}{(2\pi)^3}\omega_i. \end{aligned} \tag{11}$$

By going over to spherical variables and neglecting the vacuum contribution,

$$u_i = \frac{d\,\mathcal{U}_i}{d\nu} = \frac{4\pi^2}{c'^2}\frac{\nu^3}{e^{2\pi\nu/T} - 1}\int_0^\pi d\theta\,\frac{n_i^2}{n_o^2}\frac{\sin(\theta)}{|v_{\boldsymbol{q},i}|}. \tag{12}$$

Here $n_i = |\boldsymbol{q}|/\omega_i$ and $\boldsymbol{v}_i = \nabla_{\boldsymbol{q}}\omega_i$ stand for mode i's refraction index and group velocity, respectively. The factor $|v_{\boldsymbol{q},i}|^{-1} = |\boldsymbol{v}_i \cdot \hat{\boldsymbol{n}}|^{-1}$ is the Jacobian resulting from adopting $\nu = \omega/2\pi$ as an integration variable. The expression above resembles Planck's radiation law for dispersive anisotropic media [60,61]. Figure 1(c) shows the behavior of u_i in a DAI when $\mathfrak{b} = 5$. The frequency range covers quasiparticle energies $\omega < 10$ meV below the material's bulk gap approximately $O(0.1)$ eV as required by the low-energy description. Moreover, the sample extension $L_{x,y,z} \sim O(1)$ cm limits $|q_{x,y,z}| \gg O(10)$ μeV, providing the lowest-frequency bound $\nu_L \gg O(10^{-1})$ GHz, corresponding to $\omega \gg O(1)$ μeV [23,35], from which the results are expected to be reliable. As one could anticipate, the extraordinary spectrum shows a remarkable departure as $\nu \to m/2\pi \approx 0.48$ THz from the left, exhibiting a spectral peak whose height increases with temperature. These findings suggest that there is a characteristic temperature at which the latter becomes stronger than Wien's maximum, leading to a phase transition of the system. We will soon return to this point.

We point out that the characteristic flattening in the dispersion relation of the extraordinary mode implies that corresponding quanta with $q_\perp > m/c'$ are characterized by a perpendicular group-velocity component $v_{\perp,-} = |\partial\omega_-/\partial q_\perp| \ll c'$. Thus, in contrast to ordinary photons, the direction of energy transport of the extraordinary and axionlike modes differs from their respective wave vectors. If $\vartheta = \tan^{-1}(v_{\perp,-}/v_{\parallel,-})$ and $\theta = \tan^{-1}(q_\perp/q_\parallel)$ are the respective group and phase velocity angles relative to $\boldsymbol{B}$ with $v_{\parallel,-} = \partial\omega_-/\partial q_\parallel$, then

$$\tan(\vartheta) = \frac{v_\perp}{v_\parallel} = \tan(\theta)\frac{\omega^2\left(1 + \frac{v_s^2}{c'^2} - 2v_s^2 n_-^2\right) - m^2}{\omega^2\left(1 + \frac{v_s^2}{c'^2} - 2v_s^2 n_-^2\right) - m_*^2}, \tag{13}$$

where the results in Eq. (10) have been used. The established connection enables us to parametrically generate a graph exhibiting how the energy density due to extraordinary photons varies with the angle ϑ [solid curves in Fig. 1(d)]. Observe that the solid curves tend to be peaked at $\vartheta \approx 0$ and that this behavior is more prominent the stronger the field is. This implies that, even though the states of extraordinary quanta might be characterized by a nonzero $q_\perp$ with $m/c' < q_\perp < O(0.1)$ eV, the energy distribution occurs asymmetrically, tending to gather extraordinary photons along the $\boldsymbol{B}$ axis. A similar effect is known in QED and has since proven crucial for understanding the photon capture effect and its role within the emission mechanism of pulsars [62–64].

To assess the consequence of this effect, we have examined the spectral fluxes $\mathfrak{s}_{\parallel,\perp} = \frac{1}{V}\frac{dI_{\parallel,\perp}}{d\nu}$ parallel and perpendicular to $\boldsymbol{B}$ with $I_{\parallel,\perp}$ denoting the corresponding radiation intensities. The previous quantities are linked to the Cartesian components of the microscopic Poynting vectors ($\boldsymbol{s}_i = \omega_i\boldsymbol{v}_i$) of each propagating mode and indeed decompose $\mathfrak{s}_{\parallel,\perp} = \sum_i s_{\parallel,\perp,i}$

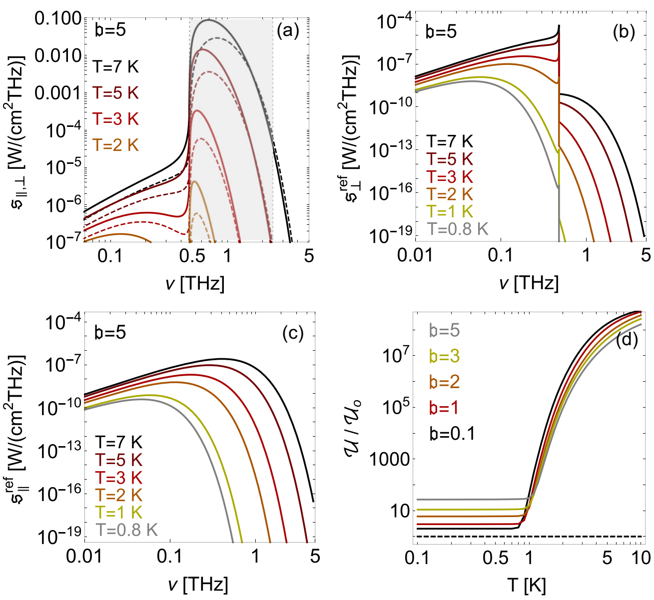

FIG. 2. (a) Spectral intensity distributions parallel (solid) and perpendicular (dashed) to $\boldsymbol{B}$ at $\mathfrak{b} = 5$ for different temperatures. The gray band shows the maximum frequency gap. Also shown is the spectral intensity (b) perpendicular and (c) parallel to the magnetic-field direction, which can undergo refraction at the DAI-vacuum interface. (d) Dependence of internal energy density $\mathcal{U}$ on the system's temperature for various magnetic fields. The dashed line gives for comparison a ratio of unity.

with

$$\mathfrak{s}_{\parallel,\perp,i} = \frac{2\pi}{c'^2}\frac{\nu^3}{e^{2\pi\nu/T}-1}\int_{\Sigma_{\parallel,\perp}} d\Omega\,\frac{n_i^2}{n_o^2}\frac{v_{\parallel,\perp,i}}{|v_{q,i}|}. \tag{14}$$

Here $d\Omega \equiv d\varphi d\cos(\theta)$ is an element of the solid angle and $\Sigma_{\parallel,\perp}$ are the corresponding integration regions, chosen so that the group-velocity components are positive (see the Appendix). The T dependence of $\mathfrak{s}_\parallel$ (solid curves) and $\mathfrak{s}_\perp \equiv \mathfrak{s}_x = \mathfrak{s}_y$ (dashed curves) is shown in Fig. 2(a) for $\mathfrak{b} = 5$. For a particular temperature, $\mathfrak{s}_\parallel$ and $\mathfrak{s}_\perp$ are qualitatively comparable but quantitatively different. The behaviors shown in Fig. 2(a) must be distinguished from the corresponding portions that may refract at the DAI-vacuum interfaces and, as a result, be detected [see Figs. 2(b) and 2(c)]. The critical angles for internal reflections related to the ordinary and extraordinary photons, both parallel and perpendicular to the magnetic field, play important roles in achieving these results (see details in the Appendix). In contrast to those associated with ordinary radiation, the ones linked to extraordinary thermal photons are dependent on ω. For $\nu < 0.48$ THz ($\omega < m$), no angular restrictions occur on $\mathfrak{s}_\perp^{\rm ref}$, and all extraordinary quanta can undergo refraction at the DAI-vacuum interface, which is perpendicular to the x axis. The fact that the corresponding sector in Fig. 2(b) matches that of Fig. 2(a) indicates that in the infrared regime, the vast majority of the refracted radiation through the latter plane is of extraordinary origin. The situation is different when $\nu \geqslant 0.48$ THz ($\omega \geqslant m$). In this case, $\mathfrak{s}_\perp^{\rm ref}$ is dominated by ordinary photons because the integration over θ in the extraordinary contribution is constrained to an infinitesimal region. This justifies the abrupt change exhibited in Fig. 2(a) close to $\nu = 0.48$ THz.

Unlike Fig. 2(b), Fig. 2(c) shows that the behavior of $\mathfrak{s}_\parallel^{\rm ref}$ resembles the classical blackbody shape. A direct comparison with the result presented in the right sector ($\nu \geqslant 0.48$ THz) of Fig. 2 indicates that the spectral intensity along $\boldsymbol{B}$, which may undergo refraction at the DAI-vacuum interface, predominantly originates from extraordinary quanta. That $\mathfrak{s}_\perp^{\rm ref}$ and $\mathfrak{s}_\parallel^{\rm ref}$ differ from each other indicates that the emission of thermal radiation from the material is also anisotropic. Thus, photon detection parallel and perpendicular to $\boldsymbol{B}$ will occur at different rates, providing indirect confirmation of the internal DAI features. Measurements might be conducted using microbolometers based on superconducting nanowires, which are projected to energy-resolve single-photon detection as low as 0.12 THz [65,66]. At $T = 7$ K, $\mathfrak{b} = 5$, ω slightly below 2 meV, and assuming a detection area $A \sim \mu\text{m}^2$, we estimate maximum output powers of $P_\parallel = I_\parallel A \sim 2\times10^{-15}$ W and $P_\perp = I_\perp A \approx 10 P_\parallel$, corresponding to upper bounds of 6 and 60 emitted photons per microsecond, respectively.

We remark that the fact that $\mathfrak{s}_\perp^{\rm ref}$ maximizes near $\omega \sim m$ for certain temperatures, accomplishing the accepted criterion $T \ll \omega$ for high sensitivity levels in DAI-based searches for axion dark matter [34,35], highlights the significance of blackbody radiation for the planned experimental setups for $T \sim O(1)$ K. Indeed, our analysis predicts that, for such temperatures, a background of thermal photons with frequency near the detection frequency $\omega \sim m_*$ could affect their discovery potential based on photon counting. This difficulty can be minimized by performing measurements at much lower temperatures $T \sim O(10^{-2})$ K where single-photon detection in the terahertz regime is still possible [67].

B. Condensation of slow thermal light

As the area below the extraordinary spectrum [see Fig. 1(c)] increases with temperature, its contribution to the energy density outweighs those of the remaining propagation modes. Figure 2(d) exhibits the T dependence of the total energy density in units of $\mathcal{U}_o = \frac{8\pi^2}{c'^3}\int_{\nu_L}^{\nu_\Lambda}\frac{d\nu\,\nu^3}{\exp(2\pi\nu/T)-1}$ for magnetic-field strengths that fall into the range permitted in the nontrivial topological phase [46]. To meet the limitations outlined below Eq. (12), the lowest integration limit here and in the contribution of the extraordinary mode was taken as $\nu_L = 10$ GHz, whereas $\nu_\Lambda = 10\ \text{meV}/2\pi$ follows from the highest energy cutoff. The findings indicate a crossover at $0.89\ \text{K} \leqslant T_c \leqslant 1.03$ K between regions with different phenomenologies. The existence of a critical temperature is confirmed by matching the thermal de Broglie wavelength $\lambda_{\rm dB} = 2\pi/\langle|\boldsymbol{q}|\rangle$ and the characteristic distance between the extraordinary photons $\xi \approx (V/N_-)^{1/3}$ [see Fig. 3(a)]. The intersections of the horizontal dashed line and the solid curves confirm the existence of critical temperatures. Deriving an approximate expression for T_c is a challenging endeavor due to the complicated nature of the dispersion relation and its B dependence. However, a numerical evaluation is shown in Fig. 3(b), which reveals a nonlinear dependence on N_- and B.

Returning to Fig. 2(d), for $\lambda_{\rm dB} > \xi$, corresponding to $T < T_c$, $\mathcal{U}_- + \mathcal{U}_+ \approx \mathcal{U}_- \approx \mathcal{C}\,\mathcal{U}_o$, where $\mathcal{C}$ is a B-dependent constant because, at lower temperatures, the area below the

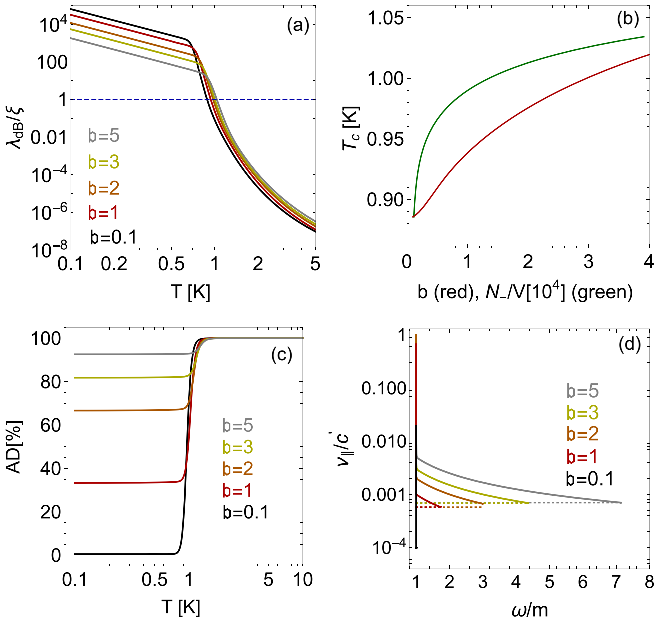

FIG. 3. (a) Dependence of the ratio between the thermal de Broglie wavelength and the interparticle distance with temperature for various field strengths. (b) Critical temperature as a function of the magnetic-field parameter (red) and the density of extraordinary photons (green). (c) Asymmetry degree of heat radiation in DAI vs temperature for different $\mathfrak{b}$. (d) Behavior of the group-velocity component of extraordinary photons along the magnetic field for $\omega \geqslant \gamma m$.

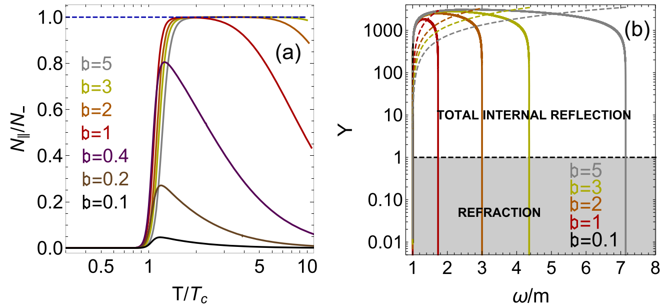

FIG. 4. (a) Condensate fraction of extraordinary photons occupying slow light states as a function of temperature for various $\mathfrak{b}$'s. (b) Dependence of Snell's law with the frequency ω at $\theta = \theta'$. For the solid curves, the label must be understood as $\Upsilon \equiv n'_- \sin(\theta')$, whereas for the dashed ones, it is $\Upsilon \equiv n'_- \cos(\theta')$.

extraordinary spectrum [see Fig. 1(c)] is still dominated by a Planck profile, although dressed by the factor $n_-^2/|v_{q,-}|$. The T scaling of $\mathcal{U}_-$ for $T > T_c$, corresponding to $\lambda_{dB} < \xi$, is however significantly stronger than $\mathcal{U}_o \approx \pi^2 T^4/30c'^3$, outweighing the contribution of the ordinary photon gas by various orders of magnitude. This indicates that the number of extraordinary photons exceeds the ordinary ones. This statement is supported by Fig. 3(c), which shows the asymmetry degree (AD) equal to $(N_- - N_o)/(N_- + N_o)$, with

$$N_i = \frac{2\pi V}{c'^2}\int_{\nu_L}^{\nu_\Lambda} \frac{d\nu\, \nu^2}{\exp(2\pi\nu/T)-1}\int_0^\pi \frac{d\theta \sin(\theta)}{|v_{q,i}|}\frac{n_i^2}{n_o^2}$$

defining the mean i-particle number. The AD can be controlled efficiently by the magnetic field when $T < T_c$, whereas for $T > T_c$ an almost complete asymmetry approximately equal to 100% is reached, regardless of B. Thus, for $\mathfrak{b} < 1$, the subcritical regime $T < T_c$ is a disordered phase because the photon species are in balance and have a broad spectrum. The latter feature persists for $\mathfrak{b} > 1$ and $T < T_c$, but the phase becomes asymmetric due to the strong dispersion. In contrast, an ordered phase emerges for $T > T_c$ whose phenomenology is governed by a spectral peak, with photons tending to occupy states with $v_\perp \ll v_\parallel$, i.e., $\tan(\vartheta) \ll 1$.

To further understand the described photon phases, we determined the nontrivial angle $\theta' \in [0, \pi]$ that makes the function $\tan(\vartheta) = 0$. This indeed occurs if the refraction index in Eq. (13) satisfies

$$n'_- \equiv n_-(\omega, \theta') = \frac{1}{\sqrt{2}v_s}\sqrt{1 + \frac{v_s^2}{c'^2} - \frac{m^2}{\omega^2}}, \tag{15}$$

with $\omega \geqslant m\gamma$ and $\gamma = (1 - v_s^2/c'^2)^{-1/2}$. The angle θ' follows by assuming the existence of a related momentum $|\boldsymbol{q}|' = n'_-\omega$. After substituting it into Eq. (9), we end up with

$$\sin^2(\theta') = 1 - \frac{v_s^2 n_-'^2}{\mathfrak{b}^2}\frac{\omega^2}{m^2}\left(1 - \frac{1 - \frac{m_*^2}{\omega^2}}{c'^2 v_s^2 n_-'^4}\right). \tag{16}$$

The expression above is meaningful if $0 \leqslant \sin^2(\theta') \leqslant 1$, which is guaranteed for

$$\gamma m \leqslant \omega \leqslant \gamma m\sqrt{1 + 2\mathfrak{b}^2}. \tag{17}$$

We note that this constraint is necessary but not sufficient to ensure that thermal quanta propagate along $\boldsymbol{B}$. Only if $\theta \approx \theta'$ can the condition $v_\perp \approx 0$ be guaranteed, and then the nontrivial component $v_\parallel$ behaves as shown in Fig. 3(d): At $\omega = \gamma m$ [see Eq. (17)], $v_\parallel$ reaches a maximum $v_{max} = c'$ and as ω increases rapidly falls to slow light states, approaching its minimum $v_{min} = v_s\mathfrak{b}/\sqrt{1 + 2\mathfrak{b}^2} \ll c'$ (horizontal dotted lines). Equipped with this information, we computed

$$N_\parallel = \frac{2\pi V}{c'^2}\int_{\nu_{min}}^{\nu_{max}} \frac{d\nu\, \nu^2}{e^{2\pi\nu/T}-1}\int_0^\pi d\theta \frac{n_-^2}{n_o^2}\frac{\sin(\theta)}{|v_{q,-}|}, \tag{18}$$

where $\nu_{min} = \gamma m/2\pi$ and $\nu_{max} = \gamma m(1 + 2\mathfrak{b}^2)^{1/2}/2\pi$. Equation (18) includes the narrow frequency sector around $v_\parallel \sim c'$. However, this contribution proves to be negligible compared to that of the slow thermal states.

The fraction of extraordinary quanta $N_\parallel/N_-$ that occupies this sort of low-dimensional ($v_\perp \approx 0$) macroscopic state is depicted in Fig. 4(a): For $T > T_c$, there exist magnetic fields under which the population of slow thermal light occurs abundantly, resembling a many-body condensate. It is important to note that this condensation differs from the observed Bose-Einstein condensation of photons in dye-filled microcavities [68–70] in that it consists of massless excitations occupying a state other than the ground state, while the latter comprises quanta with an effective mass generated by the cavity cutoff frequency populating the ground state. It also differs from an early theoretical proposal for slow-light Bose-Einstein condensation coexisting in thermodynamic equilibrium with a Bose-Einstein condensation of an ideal two-level atomic gas [71–73]. Taking $T = 2$ K and $\mathfrak{b} = 1$, corresponding to $B = 2.35$ T, the density of the condensate is $N_\parallel/V \approx 1.9 \times 10^8$ photons/cm^3, whereas the background of ordinary quanta is $N_o/V \approx 10^4$ photons/cm^3. The proposed heat flux measurements may disclose the phase transition through their response to temperature variations across T_c.

The existence of the condensate of slow thermal light raises the question of how it remains trapped within the material. To this end, let us consider Snell's law. When applied to the vacuum-DAI interface perpendicular to $\boldsymbol{B}$ it reads $n_{\rm vac}\sin(\theta^{\parallel}_{\rm vac}) = n_-(\omega,\theta)\sin(\theta)$, where $n_{\rm vac} = 1$. Extraordinary photons for which $v_\perp \approx 0$ are characterized by the refraction index n'_- [see Eq. (15)] and the angle θ' [see Eq. (16)]. The solid curves in Fig. 4(b) show the behavior of the corresponding refraction angle $\sin(\theta^{\parallel}_{\rm vac}) = n'_-(\omega)\sin(\theta')$ with frequency lying in the interval given in Eq. (17). According to our previous conclusion, only minuscule fractions of both fast ($v_\parallel \approx c'$) and extremely slow ($v_\parallel \approx v_{\rm min}$) photons can experience refraction and consequently escape into vacuum. In addition, Fig. 4(b) provides evidence that the predominant number of slow light states ($v_{\rm min} < v_\parallel \ll c'$) become confined within the insulator's boundary due to total internal reflection. The associated critical angle $\theta_c = \arcsin(1/n'_-)$ depends on ω. At the energy where the group velocity is minimal [upper bound in Eq. (17)], $\theta_c = \arcsin(v_s\sqrt{1+2\mathfrak{b}^2}/\mathfrak{b})$. For $\mathfrak{b} = 5$, $n'_- \approx 3.5 \times 10^3$ and $\theta_c \approx 0.3$ mrad. Next Snell's law relative to the interface parallel to $\boldsymbol{B}$ can be expressed as $n_{\rm vac}\cos(\theta^{\perp}_{\rm vac}) = n_-(\omega,\theta)\cos(\theta)$. The dashed curves in Fig. 4(b) depict that $n'_-(\omega)\cos(\theta') > 1$ across the entire ω range, indicating that photons from the condensate cannot escape to vacuum via the surface parallel to $\boldsymbol{B}$. This is consistent with the findings shown in the right sector of Fig. 2(b).

IV. CONCLUSION

The thermal radiation properties in DAIs are ruled by the strong birefringence that the axion-polariton state transfers to the statistical ensemble. Magnetic field and temperature are suitable parameters for quantum controlling the distribution, strength, and asymmetry of heat radiation in DAIs. Furthermore, they play a crucial role in manipulating the population of slow, extraordinary photons that could condense into a low-dimensional state of energy transport. The reported thermal features in DAI materials apply to both topological and trivial phases and thus underline their universality. However, we have seen that other thermodynamic quantities, such as free energy and total internal energy, are affected by the $\bar{\theta}$ value [see Eqs. (6) and (11)]. Our findings offer prospects for an out-of-contact, directionally tunable mechanism for manipulating heat radiation properties in DAIs.

Let us briefly address what to expect from the thermal radiation in the MDCDW phase of dense quark matter. Like DAIs, the Planck radiation law in this phase will be given by an expression similar to Eq. (12). However, as the axion quasiparticles of this model are massless [44,45], the takeoff of the corresponding extraordinary spectrum [see Fig. 1(c)]

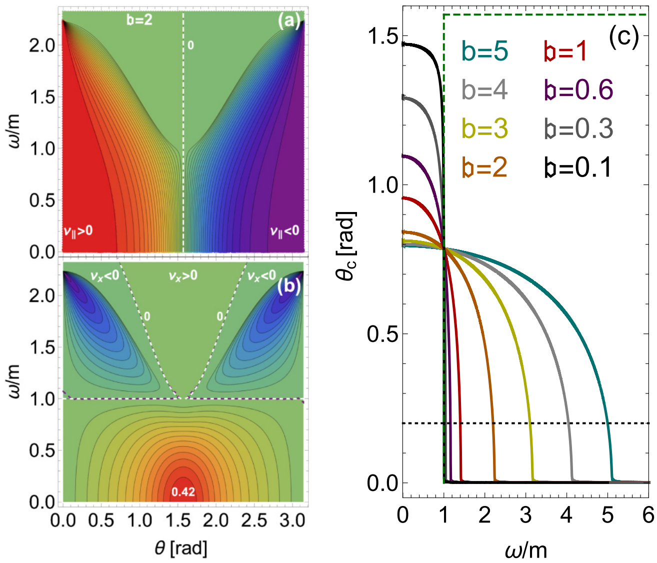

FIG. 5. Cartesian components of the extraordinary mode's group velocity (a) parallel and (b) perpendicular to the magnetic-field axis as a function of the frequency ω and the phase angle θ. (c) Critical angle for total internal reflection of the extraordinary mode parallel (solid curves) and perpendicular (green dashed curve) to the magnetic field. The latter is unaffected by the field strength and approaches zero abruptly at $\omega = m$. The horizontal dotted line represents the critical angle related to ordinary radiation.

is expected to be much more dramatic toward low frequencies, significantly exceeding that of the ordinary mode and allowing the thermal radiation to be highly asymmetric. The lack of mass renders it difficult, though, to foresee whether a peak similarly pronounced as in DAIs can emerge, along with a corresponding phase transition and condensation at the infrared. However, the anisotropic heat distribution outlined for DAIs is expected to be present in neutron star cores. A thorough investigation of these and other compelling aspects of blackbody radiation in the MDCDW phase of dense QCD is left for future work.

ACKNOWLEDGMENTS

G.Q.A. gratefully acknowledges the support of the Alexander von Humboldt Foundation. R.E. acknowledges funding from the Deutsche Forschungsgemeinschaft (German Research Foundation), under Project No. 277101999, TRR 183 (project C01), and under Germany's Excellence Strategy–Cluster of Excellence Matter and Light for Quantum Computing EXC 2004/1 Grant No. 390534769.

APPENDIX: INTEGRATION DOMAINS FOR SPECTRAL FLUXES

Consider the spectral flux $s_{\parallel,-}$ of the extraordinary mode. Here $v_{\parallel,-}$ is positive when the angular integration is limited to the upper hemisphere, i.e., when $\varphi \in [0, 2\pi)$ and $\theta \in [0, \pi/2)$. Figure 5(a) is meant to verify this statement. It shows how $v_{\parallel,-}$ behaves with ω and θ. The white dashed line indicates the contour at which $v_{\parallel,-} = 0$; on its left $v_{\parallel,-} > 0$. The situation is different for $v_{x,-}$ which follows from the first line in Eq. (10) by inserting a factor $\cos(\varphi) > 0$. As shown in Fig. 5(b), the remaining angular domain that ensures $v_{x,-} > 0$ depends on the value of ω. For $\omega \leqslant m$, the θ integration can be safety extended over the region $(0, \pi)$. However, for $\omega \geqslant m$, the θ sectors that guarantee the positive value of $v_{x,-}$ is limited by the contour $\theta'(\omega)$ [see Eq. (16)] at which $v_{x,-} = 0$ (white dashed curve). Hence, for $\omega > m$, $\mathcal{S}_{\perp,-} = \mathcal{S}_{x,-}$ has been calculated by considering $|\theta| < \theta'$. The complementary areas to this sector (covering blue hue) yield $v_{x,-} \leqslant 0$, even though $q_x = |\boldsymbol{q}| \sin(\theta) > 0$. The spectral fluxes along the $\boldsymbol{B}$ direction of mode o and $+$ can be calculated using the same domain found for $\mathcal{S}_{\parallel,-}$. Conversely, $\mathcal{S}_{\perp,o}$ and $\mathcal{S}_{\perp,+}$ follow by limiting $\varphi \in (-\pi/2, \pi/2)$ and $\theta \in (0, \pi)$.

Now the spectral flux $\mathfrak{s}_{\parallel}^{\text{ref}} = \mathcal{S}_{\parallel,o}^{\text{ref}} + \mathcal{S}_{\parallel,-}^{\text{ref}}$ that may refract at the DAI-vacuum interface perpendicular to $\boldsymbol{B}$ is obtained by integrating $\mathcal{S}_{\parallel,o}$ and $\mathcal{S}_{\parallel,-}$ over the region where $\varphi \in [0, 2\pi)$ and $\theta \in [0, \theta_{\parallel}]$. Here $\theta_{\parallel,o} = \arcsin(1/n_o) \approx 0.2$ rad is the critical angle for total internal reflection of the ordinary mode [horizontal dotted line in Fig. 5(c)], whereas $\theta_{\parallel,-}(\omega)$ is the one of the extraordinary photons. Its dependence on ω was found numerically by solving the equation $n_-(\omega, \theta) \sin(\theta) = 1$ [solid curves in Fig. 5(c)]. When calculating the spectral flux $\mathfrak{s}_{\perp}^{\text{ref}} = \mathcal{S}_{x,o}^{\text{ref}} + \mathcal{S}_{x,-}^{\text{ref}}$ that may refract at the interface perpendicular to the x axis, we considered that $\mathcal{S}_{x,o}^{\text{ref}} = \mathcal{S}_{\parallel,o}^{\text{ref}}$. The contribution of extraordinary modes $\mathcal{S}_{\perp,-}^{\text{ref}}$ depends on the frequency ω [green dashed curve in Fig. 5(c)]. For $\omega < m$, all quanta can undergo refraction. As a result, the behavior of the corresponding sector in Fig. 2(b) matches that of Fig. 2(a). For $\omega \geqslant m$, the angular integration is limited to $\varphi \in [\varphi_-, \varphi_+]$ and $\theta \in [\theta_\perp, \pi - \theta_\perp]$, where

$$\varphi_\pm = \pm \arcsin \sqrt{\frac{\cos^2(\theta_\perp) - \cos^2(\theta)}{\sin^2(\theta)}}. \tag{A1}$$

The number of photons that can be refracted is constrained here by total internal reflection, which is characterized by a critical angle $\theta_\perp$ that is determined by solving $n_-(\omega, \theta) \cos(\theta) = 1$ [green dashed curve in Fig. 5(c)]. This procedure resulted in a $\theta_\perp$ very close to $\pi/2$, limiting the θ integration to an infinitesimally small region. It prevents extraordinary photons with $\omega \geqslant m$ from refracting across the surface. Figure 2(b) summarizes the behavior of $\mathfrak{s}_{\perp}^{\text{ref}}$ with ν. It shows an abrupt change in the vicinity of $\nu = 0.48$ THz ($\omega = m$). To the left (right) of this reference value, the spectrum is dominated by extraordinary (ordinary) radiation.

[1] R. D. Peccei and H. R. Quinn, *CP* conservation in the presence of pseudoparticles, Phys. Rev. Lett. **38**, 1440 (1977).

[2] F. Wilczek, Problem of strong *P* and *T* invariance in the presence of instantons, Phys. Rev. Lett. **40**, 279 (1978).

[3] S. Weinberg, A new light boson? Phys. Rev. Lett. **40**, 223 (1978).

[4] M. Dine, W. Fischler, and M. Srednicki, A simple solution to the strong *CP* problem with a harmless axion, Phys. Lett. B **104**, 199 (1981).

[5] A. R. Zhitnitskii, On possible suppression of the axion hadron interactions, Yad. Fiz **31**, 497 (1980) [Sov. J. Nucl. Phys. **31**, 260 (1980)].

[6] J. E. Kim, Weak-interaction singlet and strong *CP* invariance, Phys. Rev. Lett. **43**, 103 (1979).

[7] M. A. Shifman, A. I. Vainshtein, and V. I. Zakharov, Can confinement ensure natural *CP* invariance of strong interactions? Nucl. Phys. B **166**, 493 (1980).

[8] K. A. Meissner and H. Nicolai, Effective action, conformal anomaly and the issue of quadratic divergences, Phys. Lett. B **660**, 260 (2008).

[9] E. Witten, Some properties of O(32) superstrings, Phys. Lett. B **149**, 351 (1984).

[10] P. Svrcek and E. Witten, Axions in string theory, J. High Energy Phys. 06 (2006) 051.

[11] O. Lebedev and S. Ramos-Sánchez, The NMSSM and string theory, Phys. Lett. B **684**, 48 (2010).

[12] M. Cicoli, M. Goodsell, and A. Ringwald, The type IIB string axiverse and its low-energy phenomenology, J. High Energy Phys. 10 (2012) 146.

[13] L. Covi, J. E. Kim, and L. Roszkowski, Axinos as cold dark matter, Phys. Rev. Lett. **82**, 4180 (1999)

[14] G. G. Raffelt, Axions: Motivation, limits and searches, J. Phys. A: Math. Theor. **40**, 6607 (2007).

[15] L. D. Duffy and K. van Bibber, Axions as dark matter particles, New J. Phys. **11**, 105008 (2009).

[16] P. Sikivie, Dark matter axions, Int. J. Mod. Phys. A **25**, 554 (2010).

[17] H. Baer, A.D. Box, and H. Summy, Neutralino versus axion/axino cold dark matter in the 19 parameter SUGRA model, J. High Energy Phys. 10 (2010) 023.

[18] T. W. Donnelly, S. J. Freedman, R. S. Lytel, R. D. Peccei, and M. Schwartz, Do axions exist? Phys. Rev. D **18**, 1607 (1978).

[19] A. Zehnder, S. J. Freedman, R. S. Lytel, R. D. Peccei, and M. Schwartz, Axion search in a monochromatic transition: A new lower limit for the axion mass, Phys. Lett. B **104**, 494 (1981).

[20] I. G. Irastorza and J. Redondo, New experimental approaches in the search for axion-like particles, Prog. Part. Nucl. Phys. **102**, 89 (2018).

[21] L. Di Luzio, M. Giannotti, E. Nardi, and L. Vasinelli, The landscape of QCD axion models, Phys. Rep. **870**, 1 (2020).

[22] F. Wilczek, Two applications of axion electrodynamics, Phys. Rev. Lett. **58**, 1799 (1987).

[23] R. Li, J. Wang, X. Qi, and S.-C. Zhang, Dynamical axion field in topological magnetic insulator, Nat. Phys. **6**, 284 (2010).

[24] Y. Gong *et al.*, Experimental realization of an intrinsic magnetic topological insulator, Chin. Phys. Lett. **36**, 076801 (2019).

[25] M. M. Otrokov *et al.*, Prediction and observation of an antiferromagnetic topological insulator, Nature (London) **576**, 416 (2019).

[26] I. I. Klimovskikh *et al.*, Tunable 3D/2D magnetism in the $(MnBi_2Te_3)(Bi_2Te_3)_m$ topological insulators family, npj Quantum Mater. **5**, 54 (2020).

[27] C. Liu, Y. Wang, H. Li, Y. Wu, Y. Li, J. Li, K. He, Y. Xu, J. Zhang, and Y. Wang, Robust axion insulator and Chern insulator phases in a two-dimensional antiferromagnetic topological insulator, Nat. Mater. **19**, 522 (2020).

[28] J.-X. Qiu, B. Ghosh, J. Schütte-Engel, *et al.*, Observation of the axion quasiparticle in 2D $MnBi_2Te_4$, Nature (London) **641**, 62 (2025).
[29] H. Ooguri, and M. Oshikawa, Instability in magnetic materials with a dynamical axion field, Phys. Rev. Lett. **108**, 161803 (2012).
[30] T. Imaeda, Y. Kawaguchi, Y. Tanaka, and M. Sato, Axion instability and nonlinear electromagnetic effect, J. Phys. Soc. Jpn. **88**, 024402 (2019).
[31] A. Sekine and K. Nomura, Chiral magnetic effect and anomalous Hall effect in antiferromagnetic insulators with spin-orbit coupling, Phys. Rev. Lett. **116**, 096401 (2016).
[32] K. Taguchi, T. Imaeda, T. Hajiri, T. Shiraishi, and Y. Tanaka, Electromagnetic effects induced by a time-dependent axion field, Phys. Rev. B **97**, 214409 (2018).
[33] A. Sekine and K. Nomura, Axion electrodynamics in topological materials, J. Appl. Phys. **129**, 141101 (2021).
[34] D. J. E. Marsh, K. C. Fong, E. W. Lentz, L. Šmejkal, and M. N. Ali, Proposal to detect dark matter using axionic topological antiferromagnets, Phys. Rev. Lett. **123**, 121601 (2019).
[35] J. Schütte-Engel, D. J. E. Marsh, A. J. Millar, A. Sekine, F. Chadha-Day, S. Hoof, M. N. Ali, K. C. Fong, E. Hardy, and L. Šmejkal, Axion quasiparticles for axion dark matter detection, J. Cosmol. Astropart. Phys. **2021**, 066 (2021).
[36] I. E. Frolov, V. C. Zhukovsky, and K. G. Klimenko, Chiral density waves in quark matter within the Nambu-Jona-Lasinio model in an external magnetic field, Phys. Rev. D **82**, 076002 (2010).
[37] E. J. Ferrer and V. de la Incera, Dissipationless Hall current in dense quark matter in a magnetic field, Phys. Lett. B **769**, 208 (2018).
[38] E. J. Ferrer and V. de la Incera, Anomalous electromagnetic transport in compact stars, Universe **4**, 54 (2017).
[39] E. J. Ferrer and V. de la Incera, Novel topological effects in dense QCD in a magnetic field, Nucl. Phys. B **931**, 192 (2018).
[40] B. Feng, E. J. Ferrer, and I. Portillo, Lack of Debye and Meissner screening in strongly magnetized quark matter at intermediate densities, Phys. Rev. D **101**, 056012 (2020).
[41] E. J. Ferrer and V. de la Incera, Magnetic dual chiral density qave: A candidate quark matter phase for the interior of neutron stars, Universe **7**, 458 (2021).
[42] W. Gyory and V. de la Incera, Phase transitions and resilience of the magnetic dual chiral density wave phase at finite temperature and density, Phys. Rev. D **106**, 016011 (2022).
[43] H. Mortazavi Ghalati and N. Sadooghi, Magnetic dual chiral density wave phase in rotating cold quark matter, Phys. Rev. D **108**, 054032 (2023).
[44] E. J. Ferrer and V. de la Incera, Axion-polariton in the magnetic dual chiral density wave phase of dense QCD, Nucl. Phys. B **994**, 116307 (2023).
[45] E. J. Ferrer and V. de la Incera, Axion-polaritons in quark stars: A possible solution to the missing pulsar problem, Eur. Phys. J. C **84**, 133 (2024).
[46] Y. Xiao, H. Wang, D. Wang, R. Lu, X. Yan, H. Guo, C. M. Hu, and K. Xia, Nonlinear level attraction of cavity axion polariton in antiferromagnetic topological insulator, Phys. Rev. B **104**, 115147 (2021).
[47] Z. L. Xiang, S. Ashhab, J. Q. You, and F. Nori, Hybrid quantum circuits: Superconducting circuits interacting with other quantum systems, Rev. Mod. Phys. **85**, 623 (2013).
[48] M. Aspelmeyer, T. J. Kippenberg, and F. Marquardt, Cavity optomechanics, Rev. Mod. Phys. **86**, 1391 (2014).
[49] Y. Xiao, H. Wang, D. Wang, X. Yan, and H. Zhang, Short-wavelength axion dark modes of cavity axion polariton, Phys. Rev. B **107**, 085109 (2023).
[50] R. J. Rivers, *Path Integral Methods in Quantum Field Theory* (Cambridge University Press, Cambridge, 1987).
[51] M. Le Bellac, *Thermal Field Theory* (Cambridge University Press, Cambridge, 1996).
[52] S. Villalba-Chávez, T. Podszus and C. Müller, Polarization-operator approach to optical signatures of axion-like particles in strong laser pulses, Phys. Lett. B **769**, 233 (2017).
[53] S. Villalba-Chávez, A. E. Shabad, and C. Müller, Magnetic dominance of axion electrodynamics: Photon capture effect and anisotropy of Coulomb potential, Eur. Phys. J. C **81**, 331 (2021).
[54] J.-M. Zhang, W. Ming, Z. Huang, G.-B. Liu, X. Kou, Y. Fan, K. L. Wang, and Y. Yao, Stability, electronic, and magnetic properties of the magnetically doped topological insulators Bi_2Se_3, Bi_2Te_3, and Sb_2Te_3, Phys. Rev. B **88**, 235131 (2013).
[55] J. Wang, B. Lian, and S.-C. Zhang, Dynamical axion field in a magnetic topological insulator superlattice, Phys. Rev. B **93**, 045115 (2016).
[56] K. Ishiwata, Axion mass in antiferromagnetic insulators, Phys. Rev. D **104**, 016004 (2021).
[57] K. Ishiwata, Topology-insensitive axion mass in magnetic topological insulators, Phys. Rev. B **106**, 195157 (2022).
[58] A. El Kanj, O. Gomonay, I. Boventer, P. Bortolotti, V. Cros, A. Anane, and R. Lebrun, Antiferromagnetic magnon spintronic based on nonreciprocal and nondegenerated ultra-fast spin-waves in the canted antiferromagnet α-Fe_2O_3, Sci. Adv. **9**, eadh1601 (2023).
[59] S. J. Pickart, M. F. Collins, and C.-G. Windsor, Spin-wave dispersion in $KMnF_3$, J. Appl. Phys. **37**, 1054 (1966).
[60] R. P. Mercier, Thermal radiation in anisotropic media, Proc. Phys. Soc. **83**, 811 (1964).
[61] K. D. Cole, Generalization of Plank's law of radiation to anisotropic dispersive media, Aust. J. Phys. **30**, 671 (1977).
[62] A. E. Shabad and V. V. Usov, Gamma-quanta capture by magnetic field and pair creation suppression in pulsars, Nature (London) **295**, 215 (1982).
[63] A. E. Shabad and V. V. Usov, Propagation of γ-radiation in strong magnetic fields of pulsars, Astrophys. Space Sci. **102**, 327 (1984).
[64] A. E. Shabad, Photon propagation in a supercritical magnetic field, J. Exp. Theor. Phys. **98**, 186 (2004).
[65] J. Wei, D. Olaya, B. S. Karasik, S. V. Pereverzev, A. V. Sergeev, and M. E. Gershenson, Ultrasensitive hot-electron nanobolometers for terahertz astrophysics, Nat. Nanotechnol. **3**, 496 (2008).
[66] B. S. Karasik, S. V. Pereverzev, A. Soibel, D. F. Santavicca, D. E. Prober, D. Olaya, and M. E. Gershenson, Energy-resolved detection of single infrared photons with $\lambda = 8$ μm using a superconducting microbolometer, Appl. Phys. Lett. **101**, 052601 (2012).
[67] S. Komiyama, O. Astafiev, V. Antonov, T. Kutsuwa, and H. Hirai, A single-photon detector in the far-infrared range, Nature (London) **403**, 405 (2000).
[68] J. Klaers, J. Schmitt, F. Vewinger, and M. Weitz, Bose-Einstein condensation of photons in an optical microcavity, Nature (London) **468**, 545 (2010).

[69] S. Barland, P. Azam, G. L. Lippi, R. A. Nyman, and R. Kaiser, Photon thermalization and a condensation phase transition in an electrically pumped semiconductor microresonator, Opt. Express **29**, 8368 (2021).
[70] J. Marelic and R. A. Nyman, Experimental evidence for inhomogeneous pumping and energy-dependent effects in photon Bose-Einstein condensation, Phys. Rev. A **91**, 033813 (2015).
[71] Y. Slyusarenko and A. Sotnikov, Green-function method in the theory of ultraslow electromagnetic waves in an ideal gas with Bose-Einstein condensates, Phys. Rev. A **78**, 053622 (2008).
[72] Y. Slyusarenko and A. Sotnikov, Role of temperature effects in the phenomenon of ultraslow electromagnetic pulses in Bose-Einstein condensates of alkali-metal atoms, Phys. Rev. A **80**, 053604 (2009).
[73] N. Boichenko and Y. Slyusarenko, Coexistence of photonic and atomic Bose-Einstein condensates in ideal atomic gases, Condens. Matter Phys. **18**, 43002 (2015).